Observations of the First Harmonic of Saturn Kilometric Radiation During Cassini's Grand Finale

Siyuan Wu, Philippe Zarka, Laurent Lamy, Ulrich Taubenschuss, Baptiste Cecconi, Shengyi Ye, Georg Fischer, William S Kurth, Théo Francez

Observations of the First Harmonic of Saturn Kilometric Radiation during Cassini's Grand Finale

Siyuan Wu[1,2], Philippe Zarka[2*], Laurent Lamy[2,3], Ulrich Taubenschuss[4], Baptiste Cecconi[2], Shengyi Ye[1*], Georg Fischer[5], William S. Kurth[6], and Théo Francez[2]

[1] Department of Earth and Space Sciences, Southern University of Science and Technology, Shenzhen, Guangdong, People's Republic of China

[2] LESIA, Observatoire de Paris, CNRS, Université PSL, Sorbonne Université, Université Paris Cité, CNRS, Meudon, France

[3] Aix-Marseille Université, CNRS, CNES, LAM, Marseille, France

[4] Department of Space Physics, Institute of Atmospheric Physics of the Czech Academy of Sciences, Prague, Czech Republic

[5] Space Research Institute, Austrian Academy of Sciences, Graz, Austria

[6] Department of Physics and Astronomy, University of Iowa, Iowa City, IA, USA

Corresponding author: Philippe Zarka (Philippe.Zarka@obspm.fr) and Shengyi Ye (yesy@sustech.edu.cn)

Key Points:

- X mode first harmonics of Saturn Kilometric Radiation (SKR) associated with X/O mode fundamental emissions are identified.
- SKR 1st harmonic occurs at frequencies very close to twice the fundamental emissions and, display weaker intensities.
- Direction-finding analysis is consistent with harmonic and fundamental emissions from the same source but affected by large uncertainties.

Abstract

Clear first harmonic emissions of Saturn Kilometric Radiation are discovered during the Cassini Grand Finale orbits. Both ordinary (O) and extraordinary (X) mode fundamental emissions accompanied by X mode harmonics are observed. Analysis shows that the frequency ratio between the fundamental and harmonic emissions is 2.01 ± 0.08, and the harmonic emissions display weaker intensities than the fundamental, by 30-40 dB for the X-X (fundamental-harmonic) type harmonic and 10-30 dB for the O-X type harmonic. The intensity relations between the two types of harmonics, i.e., O-X and X-X show different patterns that we attribute to different conditions of emission at the source. Direction-finding results shows that the fundamental and harmonic emissions are plausibly generated in the same source region. In agreement with previous studies at Earth, the generation of the two types of harmonics can be attributed to the cyclotron maser instability operating with different plasma density and electron energy distributions in the source region.

Plain Language Summary

Auroral radio emission from Saturn, namely the Saturn Kilometric Radiation (SKR), is generated along high latitude magnetic field lines via the resonance between energetic electrons and wave's electric field. This resonance mechanism is called the cyclotron maser instability. Theoretical and observational studies of the same emission at Earth, called the Auroral Kilometric Radiation (AKR), have shown that the emissions near the harmonic frequency could be generated simultaneously with the fundamental AKR emission. However, no study of SKR harmonic emissions has been reported to date. This paper focuses on searching for the possible harmonic emissions of SKR by using the data measured by the radio experiment onboard the Cassini Spacecraft. Several clear harmonic emissions are found, and their characteristics are analyzed. Based on the circular polarization, two different types of harmonic emissions are identified. We find that the harmonic emissions have a frequency exactly two times that of the fundamental emissions, but a much weaker intensity. The analysis of the source location of simultaneous fundamental and harmonic emissions suggests that they originate from the same source region. These new features of SKR observed in Saturn's magnetosphere provide new insights to the studies of cyclotron maser-related radio emissions.

1. Introduction

Saturn Kilometric Radiation (SKR) was first discovered in the 1980s during the Voyager 1 Saturn approach (Kaiser et al., 1980) before to be studied in depth by the Cassini missions (see e.g., the review of Lamy, 2017 and refs therein). The SKR mainly consists of free space Right-handed extraordinary (R-X) mode emissions within a broad frequency range, from a few kilohertz (kHz) to around one MegaHertz (MHz) (Kaiser et al., 1980, Kaiser & Desch, 1984; Lamy et al., 2008a; Kimura et al., 2013). Left-handed ordinary (L-O) mode SKR of weaker intensity was also observed in dynamic spectrograms of the SKR (Lamy et al., 2008a; Cecconi et al., 2009; Lamy et al., 2018). Like the Auroral Kilometric Radiation (AKR) at Earth (Gurnett, 1974), the SKR has been shown to be generated via the cyclotron maser instability (CMI) along auroral field lines above Saturn's polar regions (Wu & Lee. 1979; Zarka, 1998; Lamy et al., 2010, 2011, 2018; Mutel et al., 2008; Kurth et al., 2011; Menietti et al., 2011).

Harmonics of AKR as high as three times the fundamental frequencies have been observed by the ISIS 1 satellite and first reported by Benson et al. (1982). Possible O mode and X mode 1st harmonic were observed (Benson, 1982, 1984, 1985; Gurnett & Inan, 1988) and several generation mechanisms were proposed, e.g., direct generation through the CMI (Lee, Kan & Wu, 1980; Wu & Qiu, 1983; Mellott, Huff & Gurnett. 1986) or wave-wave interactions (Oya, 1990; Melrose, Hewitt & Dulk, 1984; Roux &

Pellat, 1979). The 1st harmonic described in this work is also referred to as 2nd harmonic in some of the previous works (Benson et al., 1982; Oya, 1990; Melrose, Hewitt & Dulk, 1984). In the present study we use the term "1st harmonic" in reference to the harmonic with frequency twice that of the fundamental emission, and “2nd harmonic” for the harmonic at three times the frequency of the fundamental emission.

Hosotani et al. (2003) suggested that the 1st harmonic of AKR could be observed with an occurrence up to 60% that of the observed AKR fundamental emission, and they proposed that the two mechanisms as described above may co-exist in AKR source regions because the intensity relationship between the fundamental and harmonic emissions show a linear and a quadratic trend.

Harmonic radio signals have also been tentatively observed in the Jovian magnetosphere for the Io-dependent decametric radiation and the hectometric emission related to an attenuation band, but with less convincing evidence than at Earth (Menietti & Curran, 1990; Menietti, 1995; Menietti, Gurnett & Groene, 1998).

It is thus of high interest to explore the existence of the harmonics of SKR, on which no study has been published to date, and to analyse their characteristics and generation mechanisms, in order to compare them with the various proposed generation mechanisms and document the generation of harmonic emission by the CMI. The results may have potential implications on the Jupiter CMI-related radio emissions and their possible harmonics.

Theoretical studies show that the growth rate of the harmonics is related to the parameter $\varepsilon = \frac{f_{pe}}{f_{ce}}$, with f_{pe} the electron plasma frequency and f_{ce} the electron cyclotron frequency (Lee, Kan & Wu. 1980; Wu & Qiu. 1983; Melrose, Hewitt & Dulk, 1984). The growth rates of different modes for the fundamental and harmonic emissions become dominant when the parameter ε changes. For example, when considering energetic electron distributions with a typical energy of a few keV (kilo-electron volts), the loss-cone driven CMI produces dominant X mode emissions and weak 1st harmonic (1~2 orders of magnitude weaker) also in X mode when $\varepsilon < 0.3$. When $0.3 < \varepsilon < 1$, the growth rate of fundamental O mode and harmonic X mode gradually become dominant over the fundamental X mode intensity that decreases as ε increases (Lee, Kan & Wu. 1980; Wu & Qiu. 1983). Wong, Krauss-Varban and Wu, (1989) extended the CMI mechanism to lower energy (down to a few hundred eV) electron distributions and noticed that the excitation of the dominant fundamental and harmonic emission depends on the electron energies. However, we note here that these studies are based on loss-cone electron distributions (or a DGH distribution in Wong, Krauss-Varban and Wu, (1989); DGH is a Dory–Guest–Harris distribution function that has a “hole” in the velocity plane (Dory et al., 1965)) to calculate the growth rates of the emissions, whereas horseshoe or shell distributions are rather observed in AKR and SKR source region (Treumann. 2006; Ergun et al., 2000; Lamy et al., 2018; Schippers et al., 2011). Because no study of harmonic shell-driven CMI emission is available so far, we adopted these previous results to discuss the generation mechanisms of the harmonic emissions in this study.

In this paper, we present evidence of the 1st harmonic of SKR by using the Cassini Radio and Plasma Wave Science (RPWS, Gurnett et al., 2004) data. The instrument and data are presented in Section 2. Examples are presented and the relations between fundamental and harmonic emissions are discussed in Section 3-4. A direction-finding analysis is carried out and discussed in Section 5. We discuss the results in Section 6 and summarize them in Section 7.

2. Data and Method

Cassini radio data are investigated over the orbits that brought the spacecraft at high latitudes and unprecedented close distances to Saturn and the SKR source regions, i.e. the Grand Finale and the preceding two months, from 1st Oct 2016 to 15th Sept 2017. The RPWS High Frequency Receiver (HFR) measures the wave electric field from 3.5 kHz to 16.125 MHz. The HFR spectral range is covered by logarithmically-spaced frequency channels up to 320 kHz (with a maximal resolution of 5%) and linearly-spaced frequency channels from 320 to 1825 kHz (with a maximal resolution of 12.5 kHz, Gurnett et al., 2004). This work analyses the electric field spectrogram with frequencies ranging from 100 kHz to 1800 kHz. The wave polarization data (Stokes parameter V, i.e. circular polarization degree, Kraus, 1966) used in this study are obtained from the auto- and cross-correlations of RPWS antenna signals under the assumption that the emissions are purely circularly polarized with linear polarization parameters Q=U=0 (Cecconi & Zarka, 2005; Cecconi, Lamy, & Zarka, 2017a). The direction-finding data used in Figure 4 comes from the direct inversion of the measurements of RPWS when the instrument was operating in 3-antenna mode (Cecconi & Zarka, 2005; Cecconi, Lamy, & Zarka, 2017b).

The first step of the present study is thus to identify harmonic emissions. We tested an automated algorithm based on the systematic cross-correlation of $[t_{min},t_{max}]\times[f_{min},f_{max}]$ boxes in the dynamic spectrograms of SKR with $[t_{min},t_{max}]\times[2f_{min},2f_{max}]$ boxes, but the data is too noisy (e,g, background noise, superpositions of multiple emissions) to let a significant positive correlation reveal the presence of harmonics. Therefore, we checked visually the spectrograms of SKR intensity and circular polarization to identify harmonic emissions. Our main criteria were: (1) The fundamental and harmonic emissions should be observed simultaneously on the electric field dynamic spectra, and (2) the time-frequency morphologies (shape, slope, structure) of the fundamental and harmonic emissions should be similar. Doing so, we implicitly assume that the beaming of the fundamental and harmonic emissions is similar, or else it would prevent the simultaneous detection of both components. This assumption is supported by previous calculations showing that both the fundamental and harmonic emissions can be generated with the same beaming angle (Wu & Qiu, 1983). Conversely, very different beaming angles would lead to different morphologies of fundamental and harmonic emissions on dynamic spectrograms, that would prevent the identification of the harmonic emissions. For example, if there are two identical light beams on the lighthouse illuminate the ground at different angles, the light spots on the ground will show different shapes.

To quantitatively study the frequency and intensity relationship between the identified harmonic emissions and their fundamental counterpart, we interactively and manually encircled the emissions in the dynamic spectrograms and processed the data points inside the contour lines. The noise level of the RPWS instrument in the spectral range 100 kHz-1500 kHz is a few times $10^{-18}V^2m^{-2}Hz^{-1}$ (Gurnett et al., 2004). While intense fundamental emissions can reach $10^{-10}V^2m^{-2}Hz^{-1}$, the harmonics are much weaker, down to a few $10^{-17}V^2m^{-2}Hz^{-1}$ (see section 4 for details), thus close to the background noise level. Therefore, we worked with calibrated RPWS dynamic spectra without any further processing, in order to preserve the full dynamic range of the instrument. This is why for example the interference lines at harmonics of 100 kHz, due to spacecraft power converters, are visible on these dynamic spectra (see supplementary Figures S1 to S11). The encircling process was done on an 16.9 inches pad with an electronic pencil. The drawing is by hand based on eye-inspection. To provide the raw material for this work and show the validity of our results, we display all identified cases with and without their contour lines in the supplementary Figures. Then to compute reliable spectral densities within contours (see section 4), interference lines were masked out and replaced by intensity values interpolated from nearby frequencies.

3. Observations of SKR first harmonics

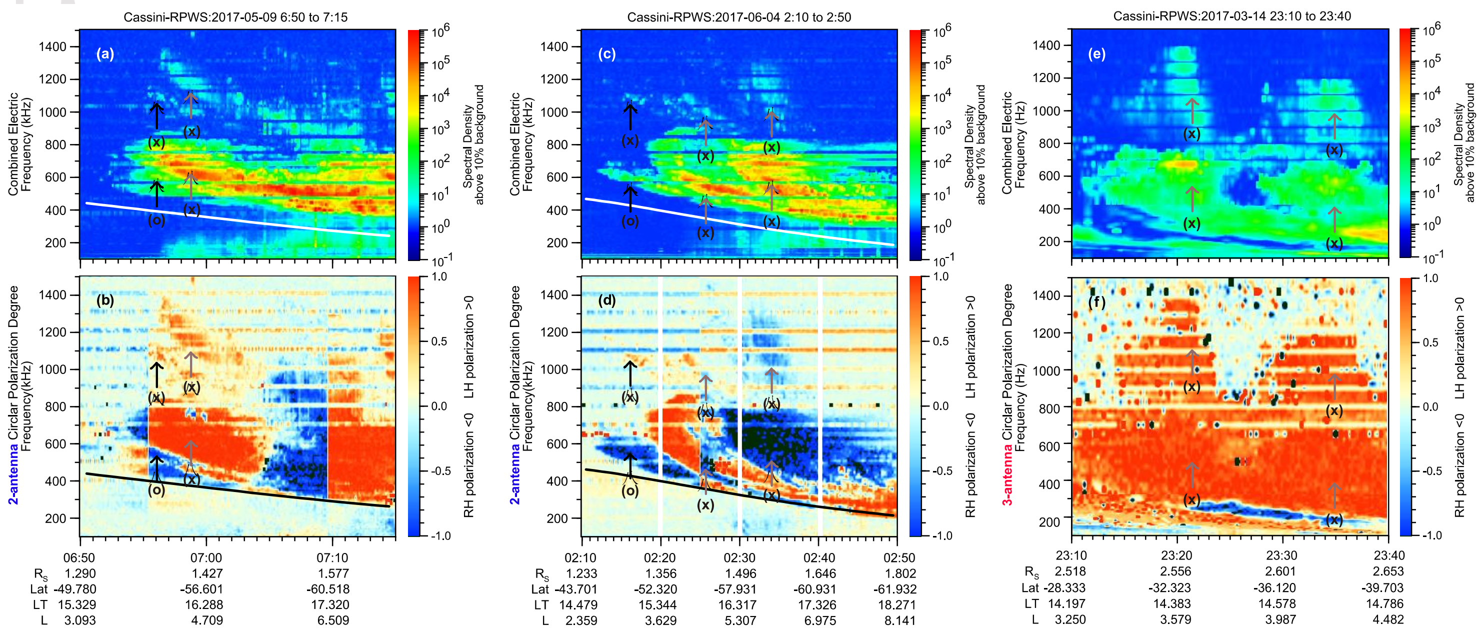

Figure 1. SKR 1st harmonics. Panels (a)–(b) display the Cassini RPWS wave electric field spectrogram in intensity and normalized circular polarization (Stokes parameter V, from −1=pure right-hand circular polarization to +1=pure left-hand circular polarization). Horizontal lines are due to spacecraft-generated interference. The white and black lines on (a)-(b) indicate the local f_{ce} at the spacecraft. Panels (c)-(d) illustrate similarly another clear occurrence on 2017/06/04. In Panels (b) and (d), the normalized Stokes parameter V is derived from two-antenna measurements via the inversion algorithm assuming thet the waves are purely circularly polarized (this sometimes leads to ambiguities and switches in V when Cassini is close to the radio source region and when the spacecraft is rolling (Cecconi & Zarka., 2005)). Panels (e)-(f) display a third observation on 2017/03/13 with Panel (f) showing the circular polarization degree V derived from three-antenna measurements (thus without ambiguity or switch). X and O mode components are labeled. The black arrows indicate O-X type harmonics (fundamental O and harmonic X modes), while the grey arrows indicate the X-X type cases.

Three observations displaying several clear harmonic cases are presented in Figure 1. A linear frequency scale is used in all Panels to illustrate the relative emission frequencies in a straightforward way. The identified harmonic emissions are mostly present above 800 kHz, and consist of several discrete structures, each of which corresponds to a different part of the fundamental emissions. The fundamental emissions associated with the harmonics usually have a stronger spectral density relative to the surrounding emissions. The intensities of harmonic emissions are weaker than the fundamental ones, and their frequency is roughly two times that of the fundamental emissions. Here, for obtaining a better display of intensities, less polluted by interference, the dynamic spectrograms in panels (a), (c) and (e) are in units of spectral density above a 10% background (the first decile of the histogram of measured intensities within each frequency channel).

The polarization data shown in Panels (b), (d) and (e) can be used to determine the magnetoionic mode of the emissions. R-X mode emissions generated in the southern hemisphere are left-hand, with a circular polarization degree close to 1 (in red), and close to -1 for L-O mode emissions from the same hemisphere (Zarka, 1998). These polarization data are derived from two-antenna or three-antenna measurements of Cassini-RPWS (Cecconi & Zarka. 2005). Only the three-antenna mode provides unambiguous polarization and thus wave mode, and this can only be obtained from time to time as shown in Panel (f). The emissions observed in the southern hemisphere with V ~ +1 (red color), as indicated by the grey arrows, suggest both the harmonic and fundamental emissions are in X mode.

Goniopolarimetric inversions using two-antenna measurements require to assume either the wave is circularly polarized, or that it is coming from the centre of Saturn. This is not always satisfied when Cassini gets close to Saturn and the SKR source regions, producing a complicated polarization pattern in two-antenna polarization data as shown in Panels (b) and (d). Cassini spacecraft rolls can produce polarization reversals when the direction of the sources passes from one side of the antenna plane to the other during the roll. The polarization reversals near UT 06:56, UT 07:10 in Panel (b) and UT 02:25 in Panel (d) are due to such rolls of Cassini since the polarization of all emissions reverses at the same time. The gradual switch of the polarization near UT 07:04 in Panel (b) is likely due to the fact that SKR sources at different frequencies, spread along Saturn field lines and emit the SKR emissions with different beaming angles, gradually pass across the Cassini-RPWS antenna plane as seen from the very close distance of Cassini (at only ~1.5 Saturn radii from Saturn's center).

In spite of the complex polarization signatures, we could identify the wave mode in all cases based on the previous reported characteristics of SKR (Lamy et al., 2008, 2011, 2018): (1) the O mode SKR is usually observed with intensities weaker than the dominant X mode SKR and at the lower frequency edge of the main emissions. (2) O mode SKR always shows circular polarization opposite to X mode SKR, in two-antenna as well as three-antenna measurements, even if the spacecraft is rolling. (3) The most intense part of SKR is X mode. For example, fundamental emissions below 600 kHz and UT 06:56 in Panels (a)-(b), indicated by the black arrows, have a weaker intensity and polarization opposite to the main SKR emissions around 600-800 kHz. This reveals O mode fundamental emission, the harmonic of which (near 900 kHz as indicated by the upper black arrow) is in X mode as it has a polarization opposite to the fundamental.

We have distinguished two types of harmonics from the observed polarization patterns. The dominant type consists of X mode harmonic emission with fundamental emission also in X mode (X-X type, indicated by the grey arrows in Figure 1), e.g., near UT 07:00 in Panel (a)-(b), after UT 02:20 in Panels (c)-(d), and all the harmonic emissions in Panels (e)-(f) as indicated by the grey arrows. The second type (14% of the cases) concerns X mode harmonic with fundamental O mode emission (O-X type, indicated by black arrows), e.g., near UT 06:56 in Panel (a)-(b), and near UT 02:17 in Panel (c)-(d).

In total, we identified 35 unambiguous cases during the Grand Finale orbits (listed in Table 1). Most cases were observed during the periapsis at high latitudes when Cassini was close to Saturn and close to the SKR source region. After a close inspection we conclude that all the harmonic emissions but two (case #23 and possibly #29) correspond to X mode, and most of them (28 cases out of 35) are accompanied by X mode fundamental emission and occasionally (5 cases out of 35) by O mode fundamental emissions, as indicated in the columns “Fundamental” and “Harmonic” in Table 1.

Table 1. SKR 1st harmonic event list and basic characteristics.

No	Start Time	End Time	Duration (min)	Lat. (°)	LT (hr)	Rs	Fundamental mode	Harmonic mode	Fundamental Normal-fitted frequency (kHz)	Harmonic Normal-fitted frequency (kHz)	Comment
1	2016/10/23 3:27	2016/10/23 3:38	11	-20.52	14.63	5.62	X	X	497.1±105.5	973.9±157.3	Possible 2nd Harmonic
2	2016/12/11 16:16	2016/12/11 16:25	9	25.61	12.63	2.76	X	X	408.5±81.7	800±96.2	Possible 2nd Harmonic
3	2016/12/11 18:48	2016/12/11 19:02	14	-37.39	12.03	2.67	X	X	495.1±96.4	977.4±170.5	
4	2016/12/26 2:51	2016/12/26 2:57	6	-34.85	14.83	2.61	X	X	481.7±92.9	976.7±102.5	
5	2017/1/9 8:25	2017/1/9 8:33	8	20.73	12.71	2.66	X	X	541.8±79.1	1066.1±129.4	Possible 2nd Harmonic
6	2017/1/9 10:27	2017/1/9 10:34	7	-29.91	14.53	2.55	X	X	536.3±78.1	1036.3±128.6	
7	2017/1/9 10:48	2017/1/9 10:57	9	-39.19	15.01	2.67	X	X	440.8±51.6	888.6±67.1	
8	2017/1/9 11:46	2017/1/9 11:48	2	-53.92	16.28	3.01	X	X	584.6±71.9	1160.5±80.3	3-antenna mode
9	2017/1/23 16:12	2017/1/23 16:14	2	21.65	12.62	2.67	X	X	415.8±27.5	877.1±24.1	
10	2017/1/23 16:16	2017/1/23 16:19	3	19.61	12.71	2.65	X	X	509.7±54.6	1001.9±75.8	
11	2017/3/7 19:10	2017/3/7 19:29	19	-30.47	14.32	2.53	X	X	492.4±55.2	981.8±73.4	Possible 2nd Harmonic
12	2017/3/14 21:09	2017/3/14 21:14	5	22.11	12.38	2.65	X	X	470±109.1	969.2±112.9	3-antenna mode
13	2017/3/14 23:18	2017/3/14 23:23	5	-32.32	14.38	2.55	X	X	557.4±98.4	1172.5±140	3-antenna mode
14	2017/3/14 23:31	2017/3/14 23:37	6	-37.97	14.68	4.22	X	X	480±97.8	1014.8±110.6	3-antenna mode
15	2017/5/9 6:55	2017/5/9 7:00	5	-54.8	16.01	1.39	O	X	489.7±42.4	1025.9±54.1	
16	2017/5/9 6:56	2017/5/9 7:03	7	-56.6	16.28	1.45	X	X	588.6±72.4	1166.1±104.3	
17	2017/6/4 2:15	2017/6/4 2:19	4	-49.1	14.91	1.32	O	X	517.6±48.9	1064.5±71.5	
18	2017/6/4 2:20	2017/6/4 2:29	9	-55.48	15.8	1.42	X	X	495.2±46	973.8±65.7	
19	2017/6/4 2:27	2017/6/4 2:36	9	-58.23	16.51	1.52	X	X	548.7±68	1084.6±115.8	
20	2017/6/17 0:44	2017/6/17 1:01	17	-61.44	17.43	1.67	X	X	572.9±95.4	1132.4±147	3-antenna mode
21	2017/6/23 11:26	2017/6/23 11:27	1	-46.01	14.42	1.24	O	X	632.1±10.7	1288.3±14.9	
22	2017/6/23 11:30	2017/6/23 11:36	6	-51.19	14.95	1.32	O	X	555.9±68.2	1121.7±89.1	
23	2017/6/23 11:36	2017/6/23 11:46	10	-56.86	15.82	1.44	X	O?	548.5±86.3	1130.2±116.1	
24	2017/6/29 23:06	2017/6/29 23:10	4	-60.16	16.695	1.59	X	X	581.8±37.9	1137.7±55.3	
25	2017/7/6 10:23	2017/7/6 10:27	4	-59.27	16.3	1.54	X	X	551.6±56.5	1145.3±91.3	3-antenna mode
26	2017/7/19 8:39	2017/7/19 8:49	10	-58.57	15.93	1.48	X	X	602.2±69	1237.1±99.1	3-antenna mode
27	2017/8/14 4:53	2017/8/14 4:56	3	-49.99	14.18	1.26	O	X	601.5±84.3	1190.1±88	

28	2017/8/14 5:01	2017/8/14 5:07	6	-59.74	15.21	1.4	X	X	620.9±116.3	1302±175.9	
29	2017/8/14 5:05	2017/8/14 5:12	7	-58.61	15.52	1.43	X	O/X?	600.3±50.4	1170.7±67.5	
30	2017/8/14 5:11	2017/8/14 5:16	5	-60.38	16.29	1.55	X	X	608.5±101.3	1209.6±163	
31	2017/8/20 16:10	2017/8/20 16:18	8	-60.22	16.12	1.53	X	X	608.2±70.3	1189.9±120.6	3-antenna mode
32	2017/8/27 3:11	2017/8/27 3:12	1	-60.51	16.28	1.55	X	X	610.4±25.9	1193.8±24.4	
33	2017/8/27 3:15	2017/8/27 3:17	2	-61.18	16.65	1.62	X	X	584.2±25.5	1166.7±34.1	
34	2017/8/27 3:17	2017/8/27 3:19	2	-61.55	17.01	1.69	X	X	585.9±49.5	1146±99.6	
35	2017/9/2 14:19	2017/9/2 14:21	2	-61.51	17.66	1.8	X	X	615.6±53.8	1252.5±46.4	

The observed harmonic emissions last from 1 to 19 minutes. All the harmonics in Table 1 are observed at frequencies higher than 600 kHz, detached from the main SKR emissions on the spectrograms. It is possible that some harmonics with lower frequency are overwhelmed by the broadband fundamental SKR emissions and cannot thus be distinguished. All these harmonic emissions are observed in the noon-dusk local time sectors, but this is where Cassini periapses lie during the Grand Finale orbits thus it is most likely an observational bias. Intriguingly, they are also observed mainly in the southern hemisphere (30 cases at latitudes between -20.5° and -61.5°) and occasionally at moderate northern latitudes (5 cases at latitudes between +19.5° and +26°). Here an observational bias is less obvious as the Grand Finale orbits are roughly symmetrical between the Northern and Southern hemispheres, but Cassini spent more time in the South when it was in the noon-dusk local time sector. The source location of the harmonic emissions may have certain local time and latitude preferences. This will be the subject of a further study (see section 7).

Beyond the harmonic examples shown in Figure 1, all identified cases are displayed, with and without superimposed contour lines (as shown in Figure 2, see next Section), in Figures S1-S11 in the Supplementary material.

4. Relationship between the fundamental and harmonic emissions

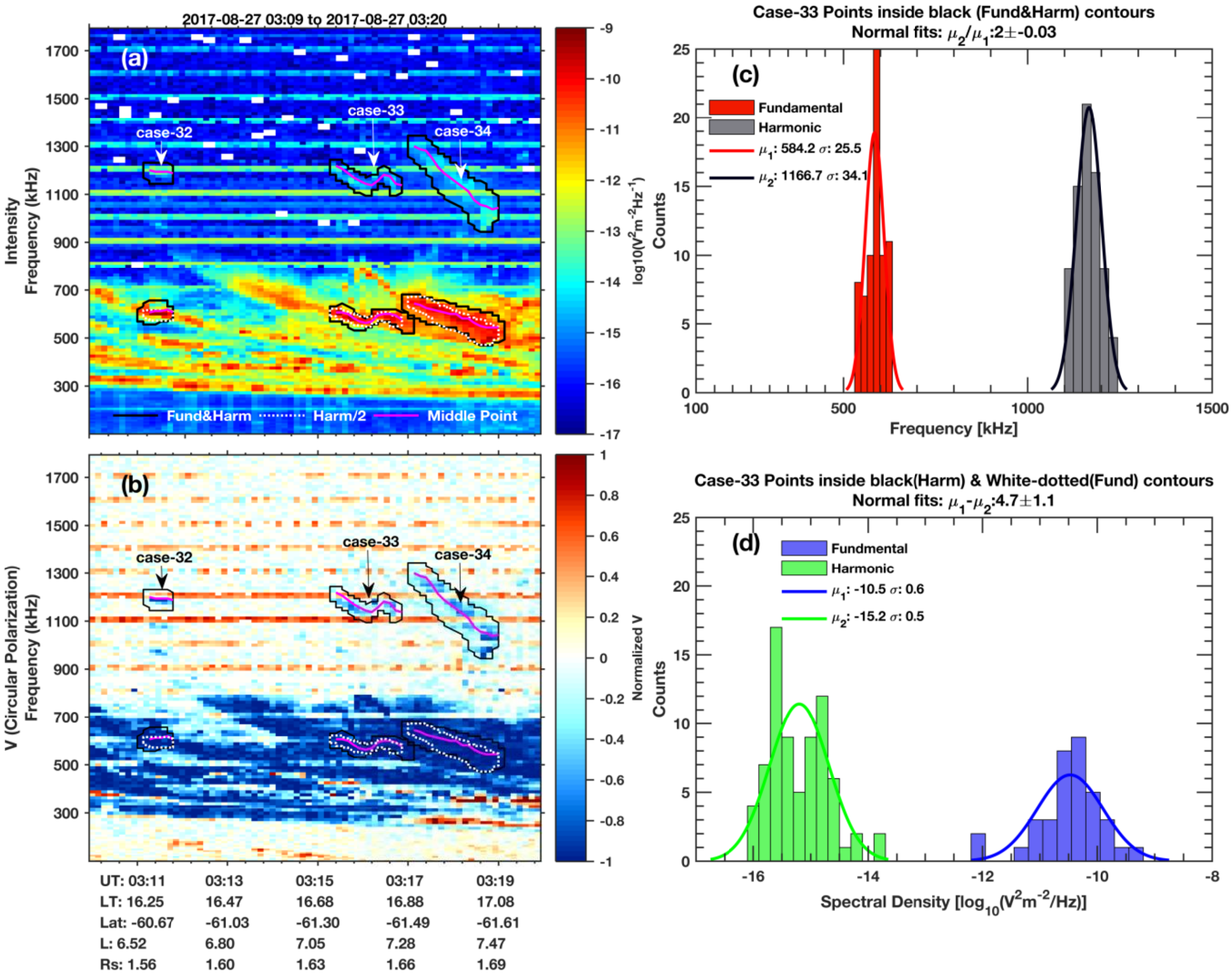

Figure 2. Examples of harmonic emissions contours. Panels (a)-(b) display the Cassini RPWS wave electric field spectrogram and normalized circular polarization for cases #32, #33, and #34 of Table 1. The black contour lines are manually plotted boundaries of the harmonic and fundamental emissions. The dotted white lines are the boundaries of the fundamental emissions derived from the black contour of harmonics (harmonic contour with frequencies divided by 2). The pink lines are the middle frequency lines of the black contours. Panels (c)-(d) display histograms of the frequencies and spectral densities of the points included in the contours of case #33. The curves in red, black, green, and blue are the normal fits of the corresponding distributions.

Panels (a)-(b) of Figure 2 illustrate the cases #32, #33, and #34 of Table 1. The black contour lines (visually and manually drawn) mark the harmonic and fundamental emissions. From the data points inside these black contours, we built the histograms and normal fit estimates of Panel (c), to test the frequency relation between the fundamental and harmonic emissions.

As shown in Panel (c) by the two fitted curves, the result show clearly that the harmonic frequency is twice that of the fundamental with the mean frequency ratios: $\frac{\mu_2 = f_{harmonic}}{\mu_1 = f_{fundmental}} = 2 \pm 0.03$. The calculated average ratio of the frequency relation based on all the 35 cases using the normal fit values is $\frac{f_{harmonic}}{f_{fundmental}} = 2.01 \pm 0.08$. Based on this result, we then re-derived the contours of the fundamental emissions from the harmonic emissions contour with frequencies divided by 2, and we obtained thus the white dotted contours displayed in Panels (a)-(b). This method allows to better isolate the fundamental emissions related to the harmonic within a broader continuum of SKR, and to analyze more accurately the intensity relation between the two components. The spectral densities inside the contour lines (black contour for the harmonic and dotted white contour for the fundamental) are then plotted in the histograms of Panel (d), after having masked out interference lines and replaced them by intensity values interpolated from nearby frequencies. Similar plots for all cases are displayed in Figures S12-S13 in the supplementary material.

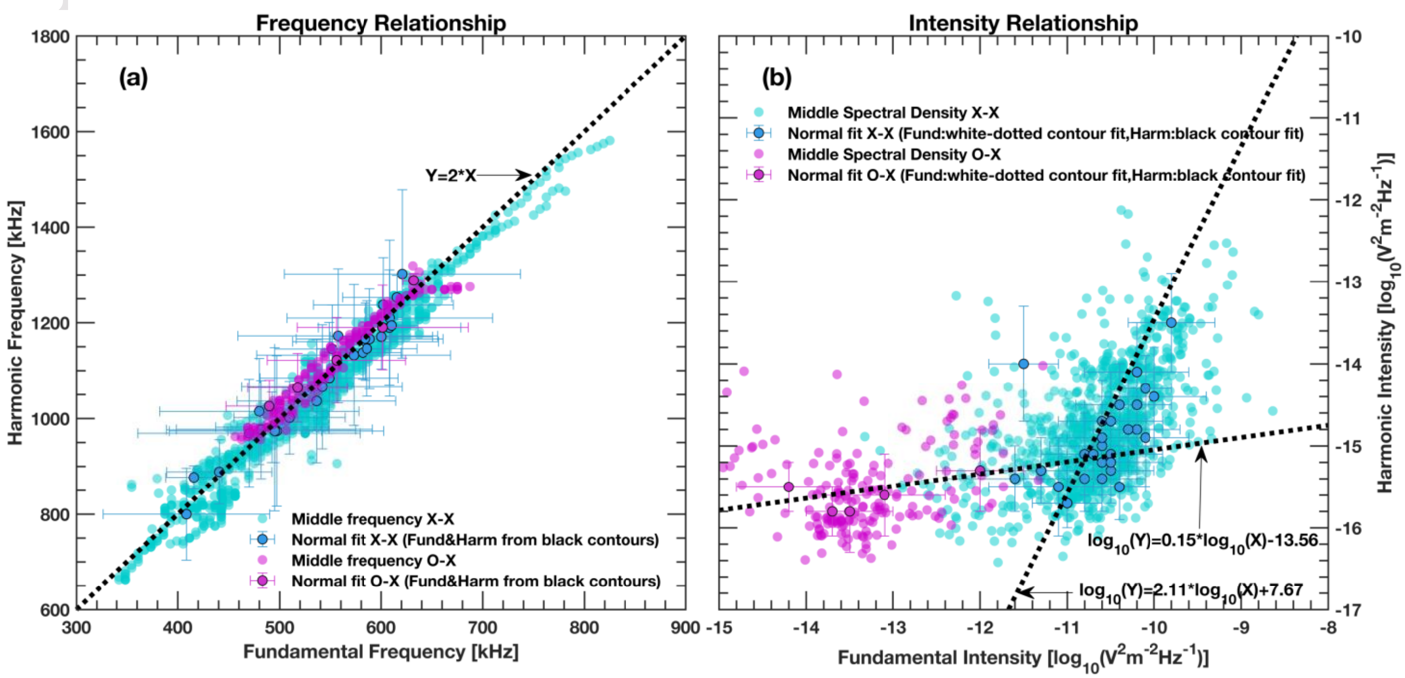

Figure 3. Relationship between the harmonic and fundamental emissions. Panels (a)-(b) show the relations between fundamental and harmonic frequencies and spectral densities for all 35 cases of Table 1. The pink and cyan dots represent the O-X (Fundamental-Harmonic) and X-X types of emissions, respectively. The dots with error bars are derived from the normal fit results as shown in Figure 2 Panels (c)-(d). The dots without an error bar are derived from the middle frequency point as indicated by the pink lines in Figure 2 Panels (a)-(b). The black dashed lines mark the relations between the fundamental and harmonic emissions.

Normal fits are derived from the histograms of each individual event to represent the average frequency and intensity of each component (fundamental and harmonic). They are shown in Figure 3 as the points with 1σ error bars. We also analyzed the frequency and spectral density along the pink lines (in Figure 2 Panels (a)-(b)) marking the middle frequencies of the contours. These series of points follow the time variations of the frequency and intensity for each individual event, and thus they could also reveal the frequency and intensity relations between components. These middle values are displayed as points without an error bar in Figure 3 Panels (a)-(b).

The factor two in frequency indicated by the Y=2*X line in Panel (a) is consistent with that obtained from the observations of AKR at Earth (Hosotani et al., 2003). We note that it is difficult to compare directly the bandwidth of the fundamental and harmonic emissions, because while the harmonic emissions are well isolated in the dynamic spectrograms, the corresponding fundamental emissions are often mixed with surrounding SKR that is not accompanied by a harmonic. On the other hand, very weak parts of the harmonic emission might fade into the noise floor of the galactic background and become invisible. We note that in most cases (Panels (a)-(b) of Figure 2 and Figures S1-S11 in the supplementary material) the white dotted contours match the morphologies of the most intense fundamental emissions, which supports the fact that the bandwidth of the harmonic emissions is also two times that of the corresponding fundamental emissions.

The pink and cyan colors in Panels (a)-(b) of Figure 3 mark the different types of harmonics: O-X and X-X. In Panel (b), the O-X and X-X harmonics tend to show different intensity ratios between harmonic and fundamental, as indicated by the two black dashed lines. These two lines are obtained by a simple least-square fit to a stright line of all the scatter points (in logarithmic values) in the panel. They are plotted to show possible power-law relations between the intensities of the two components (which would remain to be explained). The actual dependence may be more complex than a power law. One clear conclusion here is that all the harmonics are weaker than the fundamental emissions by up to 4 orders of magnitude. The O mode fundamental emissions also appear 2 to 3 orders of magnitude weaker than the X mode fundamental emissions, which is consistent with the previous study (Lamy et al., 2008a, 2011; Cecconi et al., 2009). The different intensity relations should be connected to the growth rate of the various components, and thus to the generation mechanisms or conditions of the different modes and harmonics (discussed in section 6).

5. Direction-finding analysis of the harmonic emission

In Table 1, for 8 cases among the 35 identified harmonic emissions, three-antenna mode measurements are available, which make it possible to analyze the direction of arrival of the observed emissions.

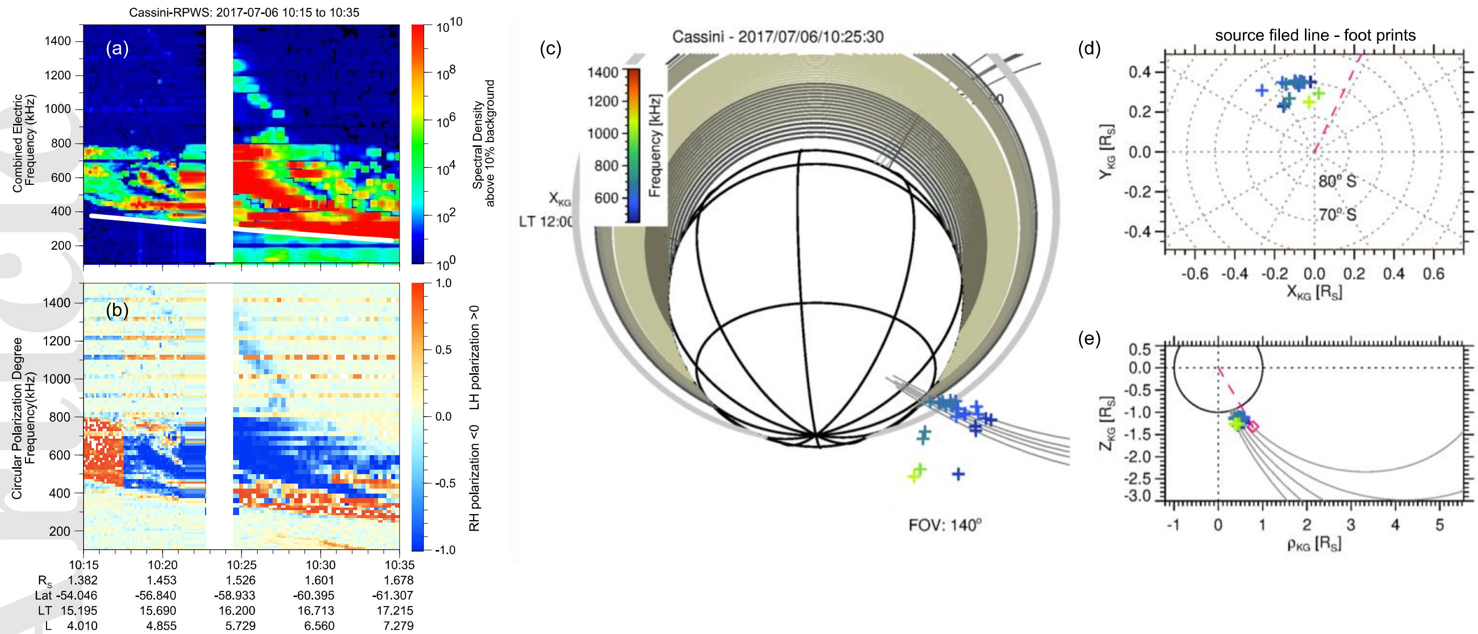

Figure 4. Direction-finding analysis of Case #25 of Table 1. Panels (a)-(b) display the wave electric field spectrogram in intensity and normalized circular polarization in the same format as Figure 1. Panels (c)-(e) show the projections of the source regions of both the harmonic and fundamental emissions (c) on the plane of the sky (d) onto the planetary surface, and (e) in a meridional plane. Each cross represents one emission source observed in one time-frequency pixel of panels (a)-(b). Their colors vary with the frequency of the emission, allowing us to separate fundamental and harmonic components. In panel (c)-(d), lines of latitude and longitude are displayed on Saturn's surface. On panels (d)-(e), the pink dashed line indicates the direction of Cassini at the time of the measurements, and the position of Cassini is represented by the pink diamond on panel (e).

The Cassini RPWS instrument has goniopolarimetric capabilities in its three-antenna mode, i.e. simultaneous polarization and direction-finding (k-vector determination) measurements of the incoming radio waves (Gurnett et al., 2004; Cecconi & Zarka. 2005). In Table 1, for 8 cases (indicated in the "Comment" colomn) among the 35 identified harmonic emissions, three-antenna mode measurements are available. We analysed all of these 8 cases and only 1 of them, shown in Figure 4, provides interpretable results. This is mainly due to the low intensity of the harmonic emissions, well below the optimal requirement of the direction-finding inversion, that the wave intensity should be at least 20 dB above the background noise (Cecconi & Zarka, 2005; Ye et al., 2009). In the case of SKR harmonics, the signal-to-noise ratio (SNR) is only a few dB, thus the directions of arrival of the wave are broadly scattered in all cases except the one displayed in Figure 4, for which the SNR was at least 3.5 dB.

Panels (a)-(b) of Figure 4 show the usual dynamic spectrograms for case #25, where the harmonic emissions are observed from UT 10:23 to UT 10:28 and both the fundamental and harmonic emissions are in X mode. Cassini was only ~1.5 Saturn Radii to Saturn's center at that time. The wave incoming directions (rays) are prolonged as straight lines (assuming thus straight-line propagation, that is justified at high latitudes where the plasma density is low), and the point at which the ray meets an electron cyclotron frequency equal to the observed frequency is taken as the source of the fundamental emission.

Conversely, direction vectors obtained for the first harmonic emission are intercepted with an fce-isosurface equaling half of the observed wave frequency.

These 3D locations are projected on the plane of the sky using a fish-eye projection in Panel (c) of Figure 4 together with a representation of the planet, its rings, and a set of magnetic field lines from a dipole model consistent with the group of source locations found. The crosses in different color represent the source positions determined at different frequencies. In total of 24 time-frequency measurements from panels (a)-(b) led to corresponding 3D source determinations, and 22 of them (bluish crosses) correspond to the fundamental emission in the frequency range 450-700 kHz and 2 sources (green crosses) to the harmonic emission in the frequency range 900-1400 kHz. In panel (d) these sources are projected along Saturn's magnetic field lines onto the surface of Saturn (in the southern hemisphere). In panel (e) they are projected into the magnetic meridian plane. The radius vector of Cassini is indicated by a pink dashed line. Although there are some deviations in Panels (c) and (d) between the light green crosses and the group of the blue crosses, one can easily notice that all crosses are roughly concentrated in a similar region. This is even more true in Panel (e).

This direction-finding analysis is subject to uncertainties due to the weakness of the signal, and it is difficult to quantify the error accurately. Nevertheless, as illustrated in Figure 9 of Cecconi and Zarka, (2005), the error in the derived angular source direction when SNR=10 dB at all Beta angles (noted α_z in Cecconi & Zarka, 2005) varies between 10° and 40° at 50 % probability level. The error decreases to 10° to 20° when Beta becomes larger than 20°. The case #25 displayed in Figure 4 corresponds to a Beta angle larger than 50°, implying an error within the range of 10° to 20°. Due to the relatively small radial distance, this error translates to 0.086~0.171 Saturn radii (0.5 Rs * sin(10° to 20°) = 0.086 to 0.171) at the source, which is comparable to the dispersion of the crosses corresponding to the harmonic and fundamental emission sources. We can thus conclude for this example that the fundamental and harmonic emissions are generated in the same source region. However, the actual values of the errors for this low signal to noise ratio has not been studied explicitly, preventing us for further analysis here.

6. Discussion

When the first AKR harmonic emission study was published, it was being argued that it could be caused by an instrumental effect rather than a natural origin (Benson & Calvert, 1979). SKR harmonic emissions discussed in this study are not of instrumental origin due to the reasons below:

- The HFR hardware has a large dynamic range, and the observed harmonics correspond to fundamental emissions that are not the most intense signals measured by the HFR (if it was an instrumental effect, the most intense emissions would systematically produce harmonics).
- Numerical values of the spectral density are not "saturated" to some constant value as shown in Figure 3 Panel (b). We see that the intensity of the fundamental at times of harmonic detection covers several orders of magnitude.
- Analog hardware saturations should appear as signals all across the HFR bands; this is sometimes observed very close to perikrones. The morphology is different from the harmonics we observed.
- Receiver saturation should not display such a clear circular polarization as shown in the polarization plot in all cases.

Previous studies of the Earth's AKR suggest the possibilities of a direct excitation of the AKR harmonics (Lee, Kan and Wu, 1980; Wu and Qiu, 1983; Winglee, 1985) through the CMI. For the X-X type harmonic, it comes naturally that the X mode 1st harmonic could be generated through the CMI with a weaker intensity when the parameter $\varepsilon = \frac{f_{pe}}{f_{ce}} < 0.3$ or a stronger intensity when $\varepsilon > 0.3$ (Lee, Kan, and Wu, 1980) when compared to the fundamental emissions. All the harmonics in Table 1 are observed with intensities much weaker than the fundamental emissions as illustrated in panel (b) of Figure 3, which suggests that the harmonic emissions are excited in source regions with $\varepsilon < 0.3$, consistent with the conditions expected in SKR sources (Zarka, 1998). Lamy et al. (2010, 2018) found ε=0.05-0.09 during low-frequency SKR source crossings. For the O-X type harmonic, the calculations of Wu and Qiu (1983) have shown that simultaneous fundamental O mode emissions and harmonic X mode emissions could have similar growth rates. Therefore, one would expect the simultaneous observation of the O mode fundamental and X mode 1st harmonic emissions. The emission of fundamental O mode may additionally require $\varepsilon > 0.3$ (Wu and Qiu, 1983; Melrose, Hewitt, and Dulk, 1984). Such large values are already observed in SKR sources at 10-80 kHz SKR (Lamy et al., 2018), but there is not, so far, any extensive study of the plasma conditions at the source of O mode SKR. The later calculations of Wong, Krauss-Varban and Wu (1989) suggest another possibility: O-X type emission could also be generated in a low-density source region ($\varepsilon < 0.3$) by auroral electrons with an energy lower than 1-2 keV.

These previous studies provide reasonable frameworks for explaining the observations of the SKR harmonics in this work. However, these studies assumed loss-cone driven CMI, and results may be different for the shell driven CMI. Further interpretations will await for a theoretical study on the harmonic emissions using a shell electron distribution. We hope that the present work is a useful first step that will be complemented by future studies.

We have noted the possible observation of 2nd harmonics (i.e. at a frequency equal to 3 times the fundamental) in a few cases, as marked in the "Comment" column in Table 1, and in Figures S1, S3 and possibly S5 in the supplementary materials. The 2nd harmonic emissions tend to show opposite polarization relative to the 1st harmonics. However, these possible 2nd harmonics are rare, generally weaker than the 1st harmonics, and sometimes mixed with the 1st harmonics, making it difficult to draw further conclusions.

Beyond the observations collected during the Grand Finale orbits, a preliminary examination of dynamic spectra revealed a few tens of cases observed during the low latitude orbits in 2004-2008. The low number of cases can be attributed to the larger distance from the source regions. We show four cases observed in the equatorial regions in Figure S14. The circular polarization is hardly detectable in some cases, and the superposition of the emissions from both hemispheres (Lamy et al., 2008a, b) makes it difficult to determine the wave mode from low latitudes. We note that in Figure S14, if the fundamental emissions are in X mode, then the harmonics, with an opposite polarization, may be in O mode. The detailed study of these cases is beyond the scope of the present paper.

7. Summary

This work is presenting clear cases of SKR 1st harmonic emissions, and we study their mode relative to the corresponding fundamental emissions (i.e., the O-X type and X-X type), their frequency ranges, and the relation of the intensity of each type of harmonic with that of the fundamental. Our main conclusions are summarized as follows:

(1) A total of 35 cases of SKR 1st harmonics from the Grand Finale orbits of Cassini are identified and categorized into two types; the most frequent one associates X mode harmonic with X mode fundamental emission (86% of the cases), and the other one corresponds to occasionally observed X mode harmonic with O mode fundamental emission (14% of the cases).

(2) The harmonic emissions have frequencies and bandwidths two times that of the fundamental emissions ($\frac{f_{harmonic}}{f_{fundmental}} = 2.01 \pm 0.08$). The spectral density relations between the fundamental and

harmonic depends on the type of harmonic (O-X or X-X). X-mode harmonics are typically 30-40 dB weaker than their corresponding X-mode fundamental. X-mode harmonics are typically 10-30 dB weaker than their corresponding O-mode fundamental.

(3) Most of the harmonic emissions during the Grand Finale orbits are observed near periapses (when Cassini was close to the SKR source region) from mid- and high latitudes, mostly in the southern hemisphere.

(4) The direction-finding analysis of a case confirms the fundamental-harmonic relation as revealed by their similar wave source region but with rather large errors limited by the weak intensity of the harmonic emissions.

(5) A few cases have been detected from low latitudes in 2004-2008, that deserve an extensive statistical study based on the entire 13-year Saturn tour. A drawback of low-latitude detections is the difficulty to analyse the wave mode in 2-antenna data.

(6) A few examples (4/35≈11%) of 2nd harmonic emissions are also detected with an opposite polarization compared to the 1st harmonic.

The detection of SKR harmonics suggests that the generation of harmonic emissions via the cyclotron maser mechanism could be a universal phenomenon, observable in various magnetized plasma environments such as the Earth’s magnetosphere and giant planets’ magnetospheres.

Acknowledgments

This work was supported by the Strategic Priority Research Program of the Chinese Academy of Sciences (grant No. XDB 41000000). GF and UT acknowledge support from the FWF-GACR international project, Austria I 4559-N/20-06802L. SYW is also supported by China Scholarship Council. PZ, LL and BC acknowledge support from the PNP and PNST programmes from CNRS/INSU, and from the CNES. SYW thanks the helpful discussion of Corentin Louis, Mingzhe Liu, Minyi Long, and Zhongying Lu on this work.

The authors thank the developers of Autoplot at University of Iowa. Figures 1 have been produced with Autoplot (Faden et al., 2010). The Cassini/RPWS data displayed on the figures have been retrieved from PADC (Paris Astronomical Data Centre) using the das2 (Piker, 2017) interfaces of the MASER (Measurements, Analysis, and Simulation of Emission in the Radio range) team (Cecconi et al., 2020).

Open Research

The Cassini RPWS data used in this work were downloaded from the LESIA/Kronos collection of n3e level (goniopolarimetric inversion results obtained following the method of Cecconi & Zarka. 2005 (Cecconi et al., 2017a, access via doi link: https://doi.org/10.25935/9ZAB-FP47)) and n3b (three-antenna direction finding inversion results, Cecconi et al., 2017b, access via doi link: https://doi.org/10.25935/F8NS-0911)) level data. The obtained catalogue of all the harmonic emissions in combined with the contour lines data are available via doi link (Wu et al., 2022): https://doi.org/10.25935/T033-QS72

References

Benson, R. F., & Calvert, W. (1979). ISIS 1 observations at the source of auroral kilometric radiation. Geophysical Research Letters, 6(6), 479–482. https://doi.org/10.1029/GL006i006p00479

Benson, R. F. (1982). Harmonic auroral kilometric radiation of natural origin. Geophysical. Research Letters, 9(9), 1120–1123. https://doi.org/10.1029/GL009i009p01120

Benson, R. F. (1984). Ordinary mode auroral kilometric radiation, with harmonics, observed by ISIS 1. Radio Science, 19(02), 543–550. https://doi.org/10.1029/RS019i002p00543

Benson, R. F. (1985). Auroral kilometric radiation: Wave modes, harmonics, and source region electron density structures. Journal of Geophysical Research: Space Physics, 90(A3), 2753–2784. https://doi.org/10.1029/JA090iA03p02753

Cecconi, B., Lamy, L., & Zarka, P. (2017a). Cassini/RPWS/HFR LESIA/Kronos N3e Data Collection (Version 1.0) [Data set]. PADC. https://doi.org/10.25935/9ZAB-FP47

Cecconi, B., Lamy, L., & Zarka, P. (2017b). Cassini/RPWS/HFR LESIA/Kronos N3b Data Collection (Version 1.0) [Data set]. PADC. https://doi.org/10.25935/F8NS-0911

Cecconi, B., Lamy, L., Zarka, P., Prangé, R., Kurth, W. S., & Louarn, P. (2009). Goniopolarimetric study of the revolution 29 perikrone using the Cassini Radio and Plasma Wave Science instrument high-frequency radio receiver. Journal of Geophysical Research: Space Physics, 114(3), 1–19. https://doi.org/10.1029/2008JA013830

Cecconi, B., Loh, A., Le Sidaner, P., Savalle, R., Bonnin, X., Nguyen, Q. N., et al. (2020). MASER: A Science Ready Toolbox for Low Frequency Radio Astronomy. Data Science Journal 19, 1062. doi:10.1029/98JE01323

Cecconi, B., & Zarka, P. (2005). Direction finding and antenna calibration through analytical inversion of radio measurements performed using a system of two or three electric dipole antennas on a three-axis stabilized spacecraft. Radio Science, 40(3), 1–20. https://doi.org/10.1029/2004RS003070

Dory, R. A., G. E. Guest, and E. G. Harris, Unstable electrostatic plasmawaves propagating perpendicular to a magnetic field,Phys. Rev. Lett.,14,131, 1965. https://doi.org/10.1103/PhysRevLett.14.131

Ergun, R. E., Carlson, C. W., McFadden, J. P., Delory, G. T., Strangeway, R. J., & Pritchett, P. L. (2000). Electron-Cyclotron Maser Driven by Charged-Particle Acceleration from Magnetic Field-aligned Electric Fields. The Astrophysical Journal, 538(1), 456–466. https://doi.org/10.1086/309094

Faden, J., Weigel, R. S., Merka, J., and Friedel, R. H. W. (2010). Autoplot: a browser for scientific data on the web. Earth Sci. inform. 3, 41–49. doi:10.1007/s12145-010-0049-0

Gurnett, D. A., & Inan, U. S. (1988). Plasma wave observations with the Dynamics Explorer 1 spacecraft. Reviews of Geophysics, 26(2), 285–316. https://doi.org/10.1029/RG026i002p00285

Gurnett, D. A., Kurth, W. S., Kirchner, D. L., Hospodarsky, G. B., Averkamp, T. F., Zarka, P., et al. (2004). The Cassini Radio and Plasma Wave Investigation. Space Science Reviews, 114(1), 395–463. https://doi.org/10.1007/s11214-004-1434-0

Gurnett, D. A. (1974). The Earth as a radio source: Terrestrial kilometric radiation. Journal of Geophysical Research (1896-1977), 79(28), 4227–4238. https://doi.org/10.1029/JA079i028p04227

Hosotani, A., Ono, T., Iizima, M., Kumamoto, A., & others. (2003). Second harmonics of auroral kilometric radiation observed by the Akebono satellite. Advances in Polar Upper Atmosphere Research, 17, 146–153. http://doi.org/10.15094/00006369

Kaiser, M. L., & Desch, M. D. (1984). Radio emissions from the planets Earth, Jupiter, and Saturn. Reviews of Geophysics, 22(4), 373–384. https://doi.org/10.1029/RG022i004p00373

Kaiser, M. L., Desch, M. D., Warwick, J. W., & Pearce, J. B. (1980). Voyager detection of nonthermal radio emission from Saturn. Science, 209(4462), 1238–1240. https://doi.org/10.1126/science.209.4462.1238

Kimura, T., Lamy, L., Tao, C., Badman, S. V, Kasahara, S., Cecconi, B., et al. (2013). Long-term modulations of Saturn's auroral radio emissions by the solar wind and seasonal variations controlled by the solar ultraviolet flux. Journal of Geophysical Research: Space Physics, 118(11), 7019–7035. https://doi.org/10.1002/2013JA018833

Kraus, J. D. (1966). Radio astronomy (McGraw-Hill, New York). (pp. 116–125).

Kurth, W. ~S., Gurnett, D. ~A., Menietti, J. ~D., Mutel, R. ~L., Kivelson, M. ~G., Bunce, E. ~J., et al. (2011). A Close Encounter with a Saturn Kilometric Radiation Source Region. In H. ~O. Rucker, W. ~S. Kurth, P. Louarn, & G. Fischer (Eds.), Planetary, Solar and Heliospheric Radio Emissions (PRE VII) (pp. 75–85). https://doi.org/10.1553/PRE7s75

Lamy, L., Cecconi, B., Zarka, P., Canu, P., Schippers, P., Kurth, W. S., et al. (2011). Emission and propagation of Saturn kilometric radiation: Magnetoionic modes, beaming pattern, and polarization state. Journal of Geophysical Research: Space Physics, 116(A4). https://doi.org/10.1029/2010JA016195

Lamy, L., Schippers, P., Zarka, P., Cecconi, B., Arridge, C. S., Dougherty, M. K., et al. (2010). Properties of Saturn kilometric radiation measured within its source region. Geophysical Research Letters, 37(12). https://doi.org/10.1029/2010GL043415

Lamy, L., Zarka, P., Cecconi, B., Prangé, R., Kurth, W. S., & Gurnett, D. A. (2008a). Saturn kilometric radiation: Average and statistical properties. Journal of Geophysical Research: Space Physics, 113(A7). https://doi.org/10.1029/2007JA012900

Lamy, L., Zarka, P., Cecconi, B., Hess, S., & Prangé, R. (2008b). Modeling of Saturn kilometric radiation arcs and equatorial shadow zone. Journal of Geophysical Research: Space Physics, 113(A10). https://doi.org/10.1029/2008JA013464

Lamy, L. (2017). The Saturnian kilometric radiation before the Cassini Grand Finale. In G. Fischer, G. Mann, M. Panchenko, & P. Zarka (Eds.), Planetary Radio Emissions VIII (pp. 171–190). https://doi.org/10.1553/PRE8s171

Lamy, L., Zarka, P., Cecconi, B., Prangé, R., Kurth, W. S., Hospodarsky, G., et al. (2018). The low-frequency source of Saturn's kilometric radiation. Science, 362(6410), eaat2027. https://doi.org/10.1126/science.aat2027

Lee, L. C., Kan, J. R., & Wu, C. S. (1980). Generation of auroral kilometric radiation and the structure of auroral acceleration region. Planetary and Space Science, 28(7), 703–711. https://doi.org/10.1016/0032-0633(80)90115-4

Mellott, M. M., Huff, R. L., & Gurnett, D. A. (1986). DE 1 observations of harmonic auroral kilometric radiation. Journal of Geophysical Research: Space Physics, 91(A12), 13732–13738. https://doi.org/10.1029/JA091iA12p13732

Melrose, D. B., Hewitt, R. G., & Dulk, G. A. (1984). Electron-cyclotron maser emission: Relative growth and damping rates for different modes and harmonics. Journal of Geophysical Research: Space Physics, 89(A2), 897–904. https://doi.org/10.1029/JA089iA02p00897

Menietti, J. D. (1995). Absence of magnetic field constraints on the source region of Jovian decametric radiation. Geophysical Research Letters, 22(11), 1389–1392. https://doi.org/10.1029/95GL00702

Menietti, J. D., & Curran D. B. (1990). Instantaneous Io flux tube as the source of Jovian DAM: Possible second harmonic emissions. Journal of Geophysical Research: Space Physics, 95(A12), 21273–21280. https://doi.org/10.1029/JA095iA12p21273

Menietti, J D. Gurnett, D. A., & J B. Groene. (1998). Second harmonic hectometric radio emission at Jupiter. Geophysical Research Letters, 25(24), 4425–4428. https://doi.org/10.1029/1998GL900

Menietti, J. D., Mutel, R. L., Schippers, P., Ye, S.-Y., Gurnett, D. A., & Lamy, L. (2011). Analysis of Saturn kilometric radiation near a source center. Journal of Geophysical Research: Space Physics, 116(A12). https://doi.org/10.1029/2011JA017056

Mutel, R. L., Christopher, I. W., & Pickett, J. S. (2008). Cluster multispacecraft determination of AKR angular beaming. Geophysical Research Letters, 35(7), L07104. https://doi.org/10.1029/2008GL033377

Oya, H. (1990). Origin of Auroral Kilometric Radiation as Conversion of the Upper Hybrid Mode Plasma Waves. Proceedings of the Japan Academy, Series B, 66(7), 129–134. https://doi.org/10.2183/pjab.66.129

Piker, C. W. (2017). Das2: Interface control document. Zenodo doi:10.5281/zenodo.3588535

Roux, A., & Pellat, R. (1979). Coherent generation of the auroral kilometric radiation by nonlinear beatings between electrostatic waves. Journal of Geophysical Research: Space Physics, 84(A9), 5189–5198. https://doi.org/10.1029/JA084iA09p05189

Schippers, P., Arridge, C. S., Menietti, J. D., Gurnett, D. A., Lamy, L., Cecconi, B., et al. (2011). Auroral electron distributions within and close to the Saturn kilometric radiation source region. Journal of Geophysical Research: Space Physics, 116(A5). https://doi.org/10.1029/2011JA016461

Treumann, R. A. (2006). The electron–cyclotron maser for astrophysical application. The Astronomy and Astrophysics Review, 13(4), 229–315. https://doi.org/10.1007/s00159-006-0001-y

Winglee, R. M. (1985). Fundamental and harmonic electron cyclotron maser emission. Journal of Geophysical Research: Space Physics, 90(A10), 9663–9674. https://doi.org/10.1029/JA090iA10p09663

Wong, H. K., Krauss-Varban, D., & Wu, C. S. (1989). On the role of the energy of suprathermal electrons in the generation of auroral kilometric radiation. Journal of Geophysical Research: Space Physics, 94(A5), 5327–5336. https://doi.org/10.1029/JA094iA05p05327

Wu, C. S., & Qiu, X. M. (1983). Emissions of second-harmonic auroral kilometric radiation. Journal of Geophysical Research: Space Physics, 88(A12), 10072–10080. https://doi.org/10.1029/JA088iA12p10072

Wu, C. S., & Lee, L. C. (1979). A theory of the terrestrial kilometric radiation. The Astrophysical Journal, 230, 621–626. https://doi.org/10.1086/157120

Wu, S. Y., Zarka, P., Lamy, L., Taubenschuss, U., Cecconi, B.,Ye, S. Y., Fischer, G. (2022). Catalogue of First Harmonic Saturn Kilometric Radiation Observations during Cassini's Grand Finale (Version 1.0) [Data set]. MASER/PADC. https://doi.org/10.25935/T033-QS72

Ye, S.-Y., Gurnett, D. A., Fischer, G., Cecconi, B., Menietti, J. D., Kurth, W. S., et al. (2009). Source locations of narrowband radio emissions detected at Saturn. Journal of Geophysical Research: Space Physics, 114(A6), A06219. https://doi.org/https://doi.org/10.1029/2008JA013855

Zarka, P. (1998), Auroral radio emissions at the outer planets: Observations and theories, J. Geophys. Res., 103(E9), 20159– 20194, https://doi.org/10.1029/98JE01323.